
Large-scale optimization-based non-negative computational framework for diffusion equations: Parallel implementation and performance studies

AN E-PRINT OF THE PAPER WILL SOON BE MADE AVAILABLE ON ARXIV.

AUTHORED BY

J. CHANG

Graduate Student, University of Houston.

S. KARRA

Staff Scientist, Los Alamos National Laboratory.

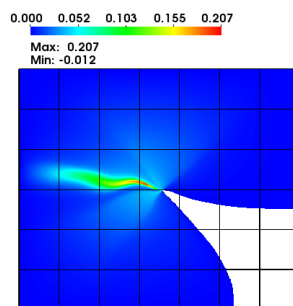
K. B. NAKSHATRALA

Department of Civil & Environmental Engineering

University of Houston, Texas 77204-4003.

phone: +1-713-743-4418, **e-mail:** knakshatrala@uh.edu

website: <http://www.cive.uh.edu/faculty/nakshatrala>



2015

COMPUTATIONAL & APPLIED MECHANICS LABORATORY

Large-scale Optimization-based Non-negative Computational Framework for Diffusion Equations: Parallel Implementation and Performance Studies

J. Chang, S. Karra and K. B. Nakshatrala

Correspondence to: *e-mail*: knakshatrala@uh.edu, *phone*:+1-713-743-4418

ABSTRACT. It is well-known that the standard Galerkin formulation, which is often the formulation of choice under the finite element method for solving self-adjoint diffusion equations, does not meet maximum principles and the non-negative constraint for anisotropic diffusion equations. Recently, optimization-based methodologies that satisfy maximum principles and the non-negative constraint for steady-state and transient diffusion-type equations have been proposed. Till date, these methodologies have been tested only on small-scale academic problems. The purpose of this paper is to systematically study the performance of the non-negative methodology in the context of high performance computing (HPC). PETSc and TAO libraries are, respectively, used for the parallel environment and optimization solvers. For large-scale problems, it is important for computational scientists to understand the computational cost, scalability and efficiency; which all will be addressed in this paper. The numerical experiments are conducted on the state-of-the-art HPC systems, and relevant parallel performance metrics are provided to illustrate the efficiency of our methodology. Our studies indicate that the proposed non-negative computational framework for diffusion-type equations exhibits excellent strong scaling for large and complicated 3D problems.

1. INTRODUCTION

The modeling of flow and transport in subsurface is vital for energy, climate and environmental applications. Examples include CO₂ migration in carbon-dioxide sequestration, enhanced geothermal systems, oil and gas production, radio-nuclide transport in a nuclear waste repository, groundwater contamination, and thermo-hydrology in the Arctic permafrost due to the recent climate change [9, 12, 14, 19]. Several numerical codes (e.g., FEHM [36], TOUGH [33], PFLOTRAN [18]) have been developed to model flow and transport in subsurface at reservoir-scale. These codes typically solve unsteady Darcy equations for flow and advection-diffusion equation for transport. The predictive capability of a numerical simulator depends on the robustness of the underlying numerical methods. A necessary and essential requirement is to satisfy important mathematical principles and physical constraints. One such property in transport and reactive-transport problems is that the concentration of a chemical species cannot be negative. Mathematically, this translates to the satisfaction of the discrete maximum principle (DMP) for diffusion-type equations. Subsurface flow and transport applications typically encounter geological media that are highly heterogeneous and anisotropic in nature, and it is well-known that

Key words and phrases. high performance computing; anisotropic diffusion; maximum principles; non-negative constraint; large-scale optimization.

the classical finite element (or finite volume and finite difference, for that matter) formulations do not produce non-negative solutions on arbitrary meshes for such porous media [6, 20, 27, 30].

Several studies over the years have focused on the development of methodologies that enforce the DMP and ensure non-negative solutions [27, 28, 30, 32]. However, these studies did not address how these methods can be used for realistic large-scale subsurface problems that have millions of grid nodes. Furthermore, complex coupling between different physical processes as well as the presence of multiple species amplify the degrees-of-freedom (i.e., the number of unknowns). The aim of this paper is to develop a parallel computational framework that solves anisotropic diffusion equations on general meshes, ensures non-negative solutions, and can be employed to solve large-scale realistic problems.

Large-scale problems can be tackled by using recent advancements in high-performance computing (HPC) methods and toolkits that can be used on the state-of-the-art supercomputing architecture. One such toolkit is PETSc [3], which provides data structures and subroutines for setting up structured and unstructured grids, parallel communication, linear and non-linear solvers, and parallel I/O. These high-level data structures and subroutines help in faster development of parallel application codes and minimizes the need to program low-level message passing, so that the domain scientists can focus more on the application. To this end, we develop a non-negative parallel framework by leveraging the existing capabilities within PETSc. Our framework ensures the DMP for anisotropic diffusion by using lower-order finite elements and the optimization approach in [20, 27, 30]. The TAO toolkit [26], that is built on top of PETSc, is used for optimization. The robustness of the proposed framework will be demonstrated by solving more realistic large-scale problems.

The rest of this paper is organized as follows. In Section 2, we present the governing equations and the classical single-field Galerkin finite element formulation for steady-state and transient diffusion equations. The optimization-based method to ensure non-negative concentrations is also outlined in this section. In Section 3, the parallel implementation procedure using PETSc and TAO is presented. We also highlight the relevant data structures used in the proposed framework, describe the performance model used to assess the efficiency of our framework, and present a pseudo algorithm describing our parallel framework. In Section 4, we first verify our implementation using a 3D benchmark problem in the literature. Then, we study a large-scale three-dimensional realistic problem involving the transport of Chromium in the subsurface and compare the numerical results of the non-negative methodology with the classical single-field Galerkin formulation. Performance metrics are also presented to illustrate the efficiency and scalability of our framework. Conclusions are drawn in Section 5.

2. GOVERNING EQUATIONS AND ASSOCIATED NON-NEGATIVE NUMERICAL METHODOLOGIES

Let $\Omega \subset \mathbb{R}^{nd}$ be a bounded open domain, where “ nd ” is the number of spatial dimensions. The boundary of the domain is denoted by $\partial\Omega = \bar{\Omega} - \Omega$, which is assumed to be piecewise smooth. A spatial point is denoted by $\mathbf{x} \in \bar{\Omega}$. The gradient and divergence operators with respect to \mathbf{x} are, respectively, denoted as $\text{grad}[\cdot]$ and $\text{div}[\cdot]$. As usual, the boundary is divided into two parts: Γ^D and Γ^N . Γ^D is that part of the boundary on which Dirichlet boundary conditions are prescribed, and Γ^N is the part of the boundary on which Neumann boundary conditions are prescribed. For mathematical well-posedness, we assume $\Gamma^D \cup \Gamma^N = \partial\Omega$ and $\Gamma^D \cap \Gamma^N = \emptyset$. The unit outward normal to boundary is denoted as $\hat{\mathbf{n}}(\mathbf{x})$. The diffusivity tensor is denoted by $\mathbf{D}(\mathbf{x})$, which is assumed to symmetric, bounded above and

uniformly elliptic. That is,

$$\mathbf{D}(\mathbf{x}) = \mathbf{D}^T(\mathbf{x}) \quad \forall \mathbf{x} \in \Omega \quad (2.1)$$

and there exists two constants $0 < \xi_1 \leq \xi_2 < +\infty$ such that

$$\xi_1 \mathbf{y}^T \mathbf{y} \leq \mathbf{y}^T \mathbf{D}(\mathbf{x}) \mathbf{y} \leq \xi_2 \mathbf{y}^T \mathbf{y} \quad \forall \mathbf{x} \in \Omega \text{ and } \forall \mathbf{y} \in \mathbb{R}^{nd} \quad (2.2)$$

2.1. Governing equations for steady-state response. We shall denote the steady-state concentration field by $c(\mathbf{x})$. The governing equations can be written as follows:

$$-\operatorname{div}[\mathbf{D}(\mathbf{x})\operatorname{grad}[c]] = f(\mathbf{x}) \quad \text{in } \Omega \quad (2.3a)$$

$$c(\mathbf{x}) = c^p(\mathbf{x}) \quad \text{on } \Gamma^D \quad (2.3b)$$

$$-\hat{\mathbf{n}}(\mathbf{x}) \cdot \mathbf{D}(\mathbf{x})\operatorname{grad}[c] = q^p(\mathbf{x}) \quad \text{on } \Gamma^N \quad (2.3c)$$

where $f(\mathbf{x})$ is the volumetric source/sink, $c^p(\mathbf{x})$ is the prescribed concentration, and $q^p(\mathbf{x})$ is the prescribed flux. For uniqueness, we assume $\Gamma^D \neq \emptyset$.

2.1.1. *Maximum principle and the non-negative constraint.* The above boundary value problem is a self-adjoint second-order elliptic partial differential equation (PDE). It is well-known that such PDEs possess an important mathematical property – the classical maximum principle [7]. The mathematical statement of the classical maximum principle can be written as follows: If $c(\mathbf{x}) \in C^2(\Omega) \cap C^0(\bar{\Omega})$, $\partial\Omega = \Gamma^D$, and $f(\mathbf{x}) \leq 0$ in Ω then

$$\max_{\mathbf{x} \in \bar{\Omega}} c(\mathbf{x}) = \max_{\mathbf{x} \in \partial\Omega} c^p(\mathbf{x}) \quad (2.4)$$

Similarly, if $f(\mathbf{x}) \geq 0$ in Ω then

$$\min_{\mathbf{x} \in \bar{\Omega}} c(\mathbf{x}) = \min_{\mathbf{x} \in \partial\Omega} c^p(\mathbf{x}) \quad (2.5)$$

To make our presentation on maximum principles simple, we have assumed stronger regularity on the solution (i.e., $c(\mathbf{x}) \in C^2 \cap C^0(\bar{\Omega})$), and assumed that Dirichlet boundary conditions are prescribed on the entire boundary. However, maximum principles requiring milder regularity conditions on the solution, even for the case when Neumann boundary conditions are prescribed on the boundary, can be found in literature (see [24, 25]).

If $f(\mathbf{x}) \geq 0$ in Ω and $c^p(\mathbf{x}) \geq 0$ on the entire $\partial\Omega$ then the maximum principle implies that $c(\mathbf{x}) \geq 0$ in the entire domain, which is the non-negativity of the concentration field.

2.1.2. *Single-field Galerkin weak formulation.* The following function spaces will be used in the rest of this paper:

$$\mathcal{U} := \{c(\mathbf{x}) \in H^1(\Omega) \mid c(\mathbf{x}) = c^p(\mathbf{x}) \text{ on } \Gamma^D\} \quad (2.6)$$

$$\mathcal{W} := \{w(\mathbf{x}) \in H^1(\Omega) \mid w(\mathbf{x}) = 0 \text{ on } \Gamma^D\} \quad (2.7)$$

where $H^1(\Omega)$ is a standard Sobolev space [1]. The single-field Galerkin weak formulation corresponding to equations (2.3a)–(2.3c) reads: Find $c(\mathbf{x}) \in \mathcal{U}$ such that we have

$$\mathcal{B}(w; c) = L(w) \quad \forall w(\mathbf{x}) \in \mathcal{W} \quad (2.8)$$

where the bilinear form and linear functional are, respectively, defined as

$$\mathcal{B}(w; c) := \int_{\Omega} \text{grad}[w(\mathbf{x})] \cdot \mathbf{D}(\mathbf{x}) \text{grad}[c(\mathbf{x})] \, d\Omega \quad (2.9a)$$

$$L(w) := \int_{\Omega} w(\mathbf{x}) f(\mathbf{x}) \, d\Omega + \int_{\Gamma^N} w(\mathbf{x}) q^p(\mathbf{x}) \, d\Gamma \quad (2.9b)$$

Since $\mathbf{D}(\mathbf{x})$ is symmetric, by Vainberg's theorem [10], the single-field Galerkin weak formulation given by equation (2.8) is equivalent to the following variational problem:

$$\underset{c(\mathbf{x}) \in \mathcal{U}}{\text{minimize}} \quad \frac{1}{2} \mathcal{B}(c; c) - L(c) \quad (2.10)$$

2.1.3. *A methodology to enforce the maximum principle for steady-state problems.* Our methodology is based on the finite element method. We decompose the domain into “*Nele*” non-overlapping open element sub-domains such that

$$\bar{\Omega} = \bigcup_{e=1}^{Nele} \bar{\Omega}^e \quad (2.11)$$

(Recall that a superposed bar denotes the set closure.) The boundary of Ω^e is denoted by $\partial\Omega^e := \bar{\Omega}^e - \Omega^e$. We shall define the following finite dimensional vector spaces of \mathcal{U} and \mathcal{W} :

$$\mathcal{U}^h := \left\{ c^h(\mathbf{x}) \in \mathcal{U} \mid c^h(\mathbf{x}) \in C^0(\bar{\Omega}), c^h(\mathbf{x})|_{\Omega^e} \in \mathbb{P}^k(\Omega^e), e = 1, \dots, Nele \right\} \quad (2.12a)$$

$$\mathcal{W}^h := \left\{ w^h(\mathbf{x}) \in \mathcal{W} \mid w^h(\mathbf{x}) \in C^0(\bar{\Omega}), w^h(\mathbf{x})|_{\Omega^e} \in \mathbb{P}^k(\Omega^e), e = 1, \dots, Nele \right\} \quad (2.12b)$$

where k is a non-negative integer, and $\mathbb{P}^k(\Omega^e)$ denotes the linear vector space spanned by polynomials up to k -th order defined on the sub-domain Ω^e . The finite element formulation for equation (2.8) can be written as: Find $c^h(\mathbf{x}) \in \mathcal{P}^h$ such that we have

$$\mathcal{B}(q^h; c^h) = L(q^h) \quad \forall q^h(\mathbf{x}) \in \mathcal{Q}^h \quad (2.13)$$

It has been documented in the literature that the above finite element formulation violates the maximum principle and the non-negative constraint [20, 27, 30].

We now outline an optimization-based methodology that satisfies the maximum principle and the non-negative constraint on general computational grids. To this end, we shall use the symbols \preceq and \succeq to denote component-wise inequalities for vectors. That is, for given any two vectors \mathbf{a} and \mathbf{b}

$$\mathbf{a} \preceq \mathbf{b} \quad \text{means that} \quad a_i \leq b_i \quad \forall i \quad (2.14)$$

The symbol \succeq can be similarly defined as well. Let $\langle \cdot; \cdot \rangle$ denote the standard inner-product in Euclidean space. After finite element discretization, the discrete equations corresponding to equation (2.13) take the form

$$\mathbf{K} \mathbf{c} = \mathbf{f} \quad (2.15)$$

where \mathbf{K} is a symmetric positive definite matrix, \mathbf{c} is the vector containing nodal concentrations, and \mathbf{f} is the force vector. Equation (2.15) is equivalent to the following minimization problem

$$\underset{\mathbf{c} \in \mathbb{R}^{ndofs}}{\text{minimize}} \quad \frac{1}{2} \langle \mathbf{c}; \mathbf{K} \mathbf{c} \rangle - \langle \mathbf{c}; \mathbf{f} \rangle \quad (2.16)$$

where “*ndofs*” denotes the number of degrees of freedom for concentration. Equation (2.15) can lead to unphysical negative solutions.

Following [20, 27], a methodology corresponding to equation (2.16) that satisfies the non-negative constraint can be written as follows:

$$\underset{\mathbf{c} \in \mathbb{R}^{ndofs}}{\text{minimize}} \quad \frac{1}{2} \langle \mathbf{c}; \mathbf{K} \mathbf{c} \rangle - \langle \mathbf{c}; \mathbf{f} \rangle \quad (2.17a)$$

$$\text{subject to} \quad \mathbf{0} \preceq \mathbf{c} \quad (2.17b)$$

where $\mathbf{0}$ is a vector of size $ndofs$ containing zeros. Since \mathbf{K} is positive definite, equation (2.17) has a unique global minimum [4]. Several robust numerical methods can be used to solve equation (2.17), which include active set strategy, interior point methods [4]. In this paper, to solve the resulting optimization problems, we shall use the parallel optimization toolkit TAO [26], which employs a quasi-Newton-based BLMVM algorithm.

2.2. Governing equations for transient response. We shall denote the time by $t \in [0, \mathcal{I}]$, where \mathcal{I} denotes the length of the time interval of interest. We shall denote the time-dependent concentration by $c(\mathbf{x}, t)$. The initial boundary value problem can be written as follows:

$$\frac{\partial c}{\partial t} = \text{div}[\mathbf{D}(\mathbf{x})\text{grad}[c]] + f(\mathbf{x}, t) \quad \text{in } \Omega \times (0, \mathcal{I}) \quad (2.18a)$$

$$c(\mathbf{x}, t) = c^P(\mathbf{x}, t) \quad \text{on } \Gamma^D \times (0, \mathcal{I}) \quad (2.18b)$$

$$-\hat{\mathbf{n}}(\mathbf{x}) \cdot \mathbf{D}(\mathbf{x})\text{grad}[c] = q^P(\mathbf{x}, t) \quad \text{on } \Gamma^N \times (0, \mathcal{I}) \quad (2.18c)$$

$$c(\mathbf{x}, 0) = c_0(\mathbf{x}) \quad \text{in } \Omega \quad (2.18d)$$

where $c_0(\mathbf{x})$ is the prescribed initial concentration, $f(\mathbf{x}, t)$ is the time-dependent volumetric source/sink, $c^P(\mathbf{x}, t)$ is the time-dependent prescribed concentration on the boundary, and $q^P(\mathbf{x}, t)$ is the prescribed time-dependent flux on the boundary.

2.2.1. Maximum principle and the non-negative constraint. The maximum principle of a transient diffusion equation asserts that the maximum can occur only on the boundary of the domain or in the initial condition if $f(\mathbf{x}, t) \geq 0$ and $\Gamma^D = \partial\Omega$. Mathematically, a solution to equations (2.18a)–(2.18a) will satisfy:

$$c(\mathbf{x}, t) \leq \max \left[\max_{\mathbf{x} \in \Omega} c_0(\mathbf{x}), \max_{\mathbf{x} \in \partial\Omega} c^P(\mathbf{x}, t) \right] \quad \forall t \quad (2.19)$$

provided $f(\mathbf{x}, t) \leq 0$. Similarly, the minimum will occur either on the boundary or in the initial condition if $f(\mathbf{x}, t) \leq 0$. That is, if $f(\mathbf{x}, t) \leq 0$ then a solution to equations (2.18a)–(2.18a) satisfies:

$$c(\mathbf{x}, t) \geq \min \left[\min_{\mathbf{x} \in \Omega} c_0(\mathbf{x}), \min_{\mathbf{x} \in \partial\Omega} c^P(\mathbf{x}, t) \right] \quad \forall t \quad (2.20)$$

If $f(\mathbf{x}, t) \geq 0$ in Ω , $c^P(\mathbf{x}, t) \geq 0$ on the entire $\partial\Omega$, and $c_0(\mathbf{x}) \geq 0$ in Ω then the maximum principle implies that $c(\mathbf{x}, t) \geq 0$ in the entire domain at all times, which is the non-negative constraint for the concentration field for transient problems.

2.2.2. A methodology to enforce the maximum principle for transient problems. We divide the time interval of interest into \mathcal{N} sub-intervals. That is,

$$[0, \mathcal{I}] := \bigcup_{n=0}^{\mathcal{N}} [t_n, t_{n+1}] \quad (2.21)$$

where t_n denotes the n -th time-level. We assume that the time-step is uniform, which can be written as:

$$\Delta t = t_{n+1} - t_n \quad (2.22)$$

Following the recommendation provided in [29] to meet maximum principles, we employ the backward Euler method for temporal discretization. We shall denote the nodal concentrations at the n -th time-level by $\mathbf{c}^{(n)}$. We shall denote the minimum and maximum values for the concentration by c_{\min} and c_{\max} , which will be provided by the maximum principle and the non-negative constraint. At each time-level, one has to solve the following convex quadratic program:

$$\underset{\mathbf{c}^{(n+1)}}{\text{minimize}} \quad \frac{1}{2} \langle \mathbf{c}^{(n+1)}; \widetilde{\mathbf{K}} \mathbf{c}^{(n+1)} \rangle - \langle \mathbf{c}^{(n+1)}; \widetilde{\mathbf{f}}^{(n+1)} \rangle \quad (2.23a)$$

$$\text{subject to} \quad c_{\min} \mathbf{1} \preceq \mathbf{c}^{(n+1)} \preceq c_{\max} \mathbf{1} \quad (2.23b)$$

where

$$\widetilde{\mathbf{K}} := \frac{1}{\Delta t} \mathbf{M} + \mathbf{K} \quad (2.24)$$

$$\widetilde{\mathbf{f}}^{(n+1)} := \mathbf{f}^{(n+1)} + \frac{1}{\Delta t} \mathbf{M} \mathbf{c}^{(n+1)} \quad (2.25)$$

In the above equation, \mathbf{M} is the capacity matrix [29].

3. PARALLEL IMPLEMENTATION

3.1. PETSc and TAO. We leverage on existing scientific libraries such as PETSc and TAO to formulate our large-scale computational framework. PETSc is a suite of data structures and routines for the parallel solution of scientific applications. It also provides interfaces to several other libraries such as Metis/ParMETIS [13] and HDF5 [34] for mesh partitioning and binary data format handling respectively. A Data Management (DM) data structure is used to manage all information including vectors and sparse matrices and compatible with binary data formats. One of the most widely used DM structures is DMDA, and it is often used for the parallel solution of problems on structured grids. To handle unstructured grids in parallel, the application developer would have to manage the grid data structure through the use of index sets and MPI related functions, but a new DM structure called DMplex (see [3]) has recently been introduced to automate this process.

The DMplex data structure is an extremely powerful API [17] for manipulating meshes and data over meshes. It can represent any unstructured grid and has support for hybrid elements and non-orientable surfaces. Moreover, it reduces all mesh or sieve points to a single covering relation. Figure 1 depicts a DMplex mesh representation as a Hasse Diagram or Directed Acyclic Graph (DAG). Each topological point can be accessed from any depth and enables computational scientists to combine and compare different discretizations for a wide array of numerical methods (e.g., finite element, finite volume, etc). By simply reading a DAG containing only cells and vertices, element edges and faces can automatically be generated. These “interpolated” meshes enable the user to use higher orders of discretization. DMplex supports important features such as load balancing, parallel I/O, and mesh refinement.

Another important feature within PETSc is TAO. The TAO library has a suite of data structures and routines that enable the solution of large-scale optimization problems. It can support any data structure or solver within PETSc. Our non-negative methodology will use the Bounded Limited-Memory Variable-Metric (BLMVM) solver within TAO. BLMVM is a quasi-Newton method and uses projected

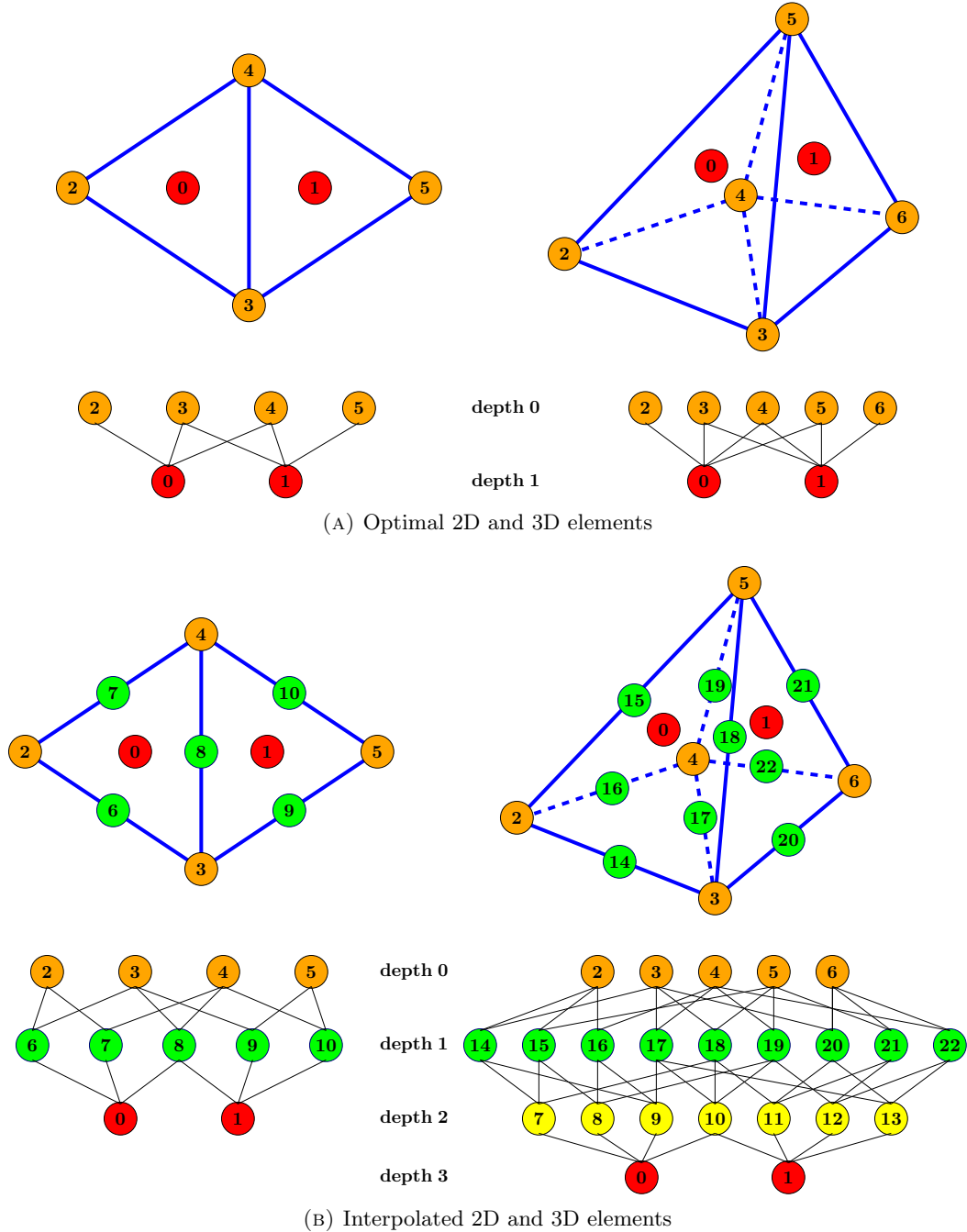


FIGURE 1. Representation of mesh points within the DMPlex data structure and their associated directed acyclic graphs

gradients to approximate the Hessian. Other popular methods available for bounded constraints include Newton-Trust Region (TRON) and Gradient Projected Conjugate Gradient (GPCG) which typically require more information, memory, and the explicit formation of a Hessian. Further details regarding the implementation of these various methods may be found in [26] and the references within.

TABLE 1. List of HPC systems used in this study

| | Mustang (MU) | Wolf (WF) |
|-----------------------------|------------------|--------------------|
| Processor | AMD Opteron 6176 | Intel Xeon E5-2670 |
| Clock rate | 2.3 GHz | 2.6 GHz |
| FLOPs/cycle | 4 | 8 |
| Sockets per compute node | 2 | 2 |
| NUMA nodes per socket | 2 | 1 |
| Cores per socket | 12 | 8 |
| Total cores (compute nodes) | 38400 (1600) | 9856 (616) |
| Memory per compute node | 64 GB | 64 GB |
| L1 cache per core | 128 KB | 32 KB |
| L2 cache per core | 512 KB | 256 KB |
| L3 cache per socket | 12 MB | 20 MB |
| Interconnect | 40 Gb/s | 40 Gb/s |
| STREAMS Triad | 5.51 GB/s | 13.38 GB/s |

3.2. Computational performance. Hardware specifications of HPC systems significantly impact the performance of any numerical algorithm. Ideally we want our simulations to consume as little wall-clock time as possible as the number of processing cores increases (i.e., achieving good speedup), but several other factors including compiler vectorization, cache usage, memory bandwidth, and code implementation may significantly hinder the overall performance. Table 1 lists the hardware specifications of the two HPC systems (Mustang and Wolf) that will be used in our numerical experiments. The STREAMS Triad benchmark [11] is widely used to compute the achievable memory performance for a given machine. The best possible metric for this benchmark on one MPI process has also been listed in Table 1. The two HPC systems are part of Los Alamos National Laboratory’s (LANL) Open Collaborative Network (Turquoise). The Mustang HPC system uses older processors and is expected to have lower computational performance than the Wolf system. For large-scale computing, wall-clock time and speedup are two of the most commonly reported metrics when analyzing the performance of any scientific code, but we also want to know how efficiently different solvers are for a given problem size across various computing platforms. The Wall-clock time of any large-scale simulation can generally be summed up as a function of three things: the workload, transfer of data between the memory and CPU register, and interprocess communication. Efficiency in this context is defined as the amount of time spent performing work over waiting on memory fetching and cache registers to free up.

The performance of many numerical methods on modern architectures is bounded on the upper side by the memory bandwidth. That is, the floating point performance given by FLOPS/s will never reach the theoretical peak performance (TPP) of a given machine. This issue becomes increasingly paramount as one employs iterative and optimization methods that rely on numerous sparse matrix-vector multiplications. These methods allow for little cache reuse and may result in very expensive cache misses. Performance and cache models such as the Roofline Model [21, 35] can be used to predict and assess the computational efficiency of a program on multi-processors. Performance models may help application developers identify bottlenecks and may indicate which parts of the code can be better optimized. The core parameter for these performance models is the Arithmetic Intensity (AI) which is computed as the ratio of total FLOPS over total DRAM bytes transferred (TBT). The AI serves as

a multiplier to the actual memory bandwidth and creates a “roofline” for the estimation of ideal peak performance.

To this end, we express the computational efficiency based on the Roofline performance model as:

$$\text{Efficiency (\%)} = \frac{\text{Measured FLOPS/s}}{\min \left\{ \begin{array}{l} \text{TPP} \\ \text{AI} \times \text{STREAMS} \end{array} \right\}} \times 100 \quad (3.1)$$

where the numerator is reported by the PETSc program and the denominator is the ideal performance upper bounded by both the TPP and the product of AI and STREAMS bandwidth. We compute the TBT for sparse matrix-vector multiplications by following the procedure outlined in [8]. The estimations of the AI rely on these key assumptions:

- All floating-point operations (add, multiply, square roots, etc.) are treated equally and equate to one FLOP count.
- There are no conflict misses. That is, each matrix and vector element is loaded into cache only once.
- Processor never waits on a memory reference. That is, any number of loads and stores are satisfied in a single cycle.
- Scalars quantities are loaded and stored only once in pure streaming computations.

It should be noted that this performance model does not deal with cache effects, that is it does not quantify the useful bandwidth sustained for some level of cache. The actual hardware or algorithmic efficiencies may not be reflected by this model, so our aim is to show relative performance between select PETSc and TAO solvers. Comparing the AI and the measured FLOPS/s with the STREAMS bandwidth will give us a better understanding of how efficiently the PETSc and TAO solvers are performing work.

3.3. Implementation. PETSc abstractions for finite elements, quadrature rules, and function spaces have also been recently introduced and are suitable for the mesh topology within DMPlex. They are built upon the same framework as the Finite element Automatic Tabulator (FIAT) found within the FEniCS Project [15, 22, 23]. The finite element discretizations simply need the equations, auxiliary coefficients (e.g., permeability, diffusivity, etc.), and boundary conditions specified as point-wise functions. We express all discretizations in nonlinear form so let \mathbf{r} and \mathbf{J} denote the residual and Jacobian respectively.

Following the FEM model outlined in [16], we consider the weak form that depends on fields and gradients. The residual evaluation can be expressed as:

$$\mathbf{w}^T \mathbf{r}(\mathbf{c}) \sim \int_{\Omega^e} [w \cdot \mathcal{F}_0(c, \nabla c) + \nabla w \cdot \mathcal{F}_1(c, \nabla c)] d\Omega = 0 \quad (3.2)$$

where $\mathcal{F}_0(c, \nabla c)$ and $\mathcal{F}_1(c, \nabla c)$ are user-defined point-wise functions that capture the problem physics. This framework decouples the problem specification from the mesh and degree of freedom traversal. That is, the scientist need only focus on providing point function evaluations while letting the finite element library take care of meshing, quadrature points, basis function evaluation, and mixed forms if any. The discretization of the residual is written as:

$$\mathbf{r}(\mathbf{c}) = \mathbf{A}_{e=1}^{N_{ele}} \left[\mathbf{N}^T \quad \mathbf{B}^T \right] \mathbf{W} \begin{bmatrix} \mathcal{F}_0(c_q, \nabla c_q) \\ \mathcal{F}_1(c_q, \nabla c_q) \end{bmatrix} \quad (3.3)$$

where \mathbf{A} represents the standard assembly operator, \mathbf{N} and \mathbf{B} are matrix forms of basis functions that reduce over quadrature points, \mathbf{W} is a diagonal matrix of quadrature weights (including the geometric Jacobian determinant of the element), and c_q is the field value at quadrature point q . The Jacobian of (3.3) needs only the derivatives of the point-wise functions:

$$\mathbf{J}(\mathbf{c}) = \mathbf{A}_{e=1}^{Nele} \begin{bmatrix} \mathbf{N}^T & \mathbf{B}^T \end{bmatrix} \mathbf{W} \begin{bmatrix} \mathcal{F}_{0,0} & \mathcal{F}_{0,1} \\ \mathcal{F}_{1,0} & \mathcal{F}_{1,1} \end{bmatrix} \begin{bmatrix} \mathbf{N} \\ \mathbf{B} \end{bmatrix}, \quad [\mathcal{F}_{i,j}] = \begin{bmatrix} \frac{\partial \mathcal{F}_0}{\partial c} & \frac{\partial \mathcal{F}_0}{\partial \nabla c} \\ \frac{\partial \mathcal{F}_1}{\partial c} & \frac{\partial \mathcal{F}_1}{\partial \nabla c} \end{bmatrix} (c_q, \nabla c_q) \quad (3.4)$$

The point-wise functions corresponding to the weak form in (2.9) would be:

$$\mathcal{F}_0 = -f(\mathbf{x}), \quad \mathcal{F}_1 = \mathbf{D}(\mathbf{x})\nabla c_q \quad (3.5a)$$

$$\mathcal{F}_{0,0} = 0, \quad \mathcal{F}_{0,1} = 0, \quad \mathcal{F}_{1,0} = \mathbf{0}, \quad \mathcal{F}_{1,1} = \mathbf{D}(\mathbf{x}) \quad (3.5b)$$

Similarly, the point-wise functions for the transient response are:

$$\mathcal{F}_0 = \dot{c}_q - f(\mathbf{x}, t), \quad \mathcal{F}_1 = \mathbf{D}(\mathbf{x})\nabla c_q \quad (3.6a)$$

$$\mathcal{F}_{0,0} = \frac{1}{\Delta t}, \quad \mathcal{F}_{0,1} = 0, \quad \mathcal{F}_{1,0} = \mathbf{0}, \quad \mathcal{F}_{1,1} = \mathbf{D}(\mathbf{x}) \quad (3.6b)$$

where \dot{c}_q denotes the time derivative. A similar discretization is used to project the Neumann boundary conditions into the residual vector. Assuming a fixed time-step, $[\mathcal{F}_{i,j}]$ and the Jacobian in equation (3.4) do not change with time and have to be computed only once. If n denotes the time level ($n = 0$

Algorithm 1 Pseudocode for the large-scale transport solver

```

Create/input DAG on rank 0
Create/input cell-wise velocity on rank 0
if size > 1 then
    Partition mesh among all processors
end if
Refine distributed mesh if necessary
Create PetscSection and FE discretization
Set  $n = 0$  and  $\mathbf{c}^{(0)} = 10^{-8}$ 
Insert Dirichlet BC constraints into  $\mathbf{c}^{(0)}$ 
Compute Jacobian  $\mathbf{J}$ 
while true do ▷ Begin time-stepping scheme
    Compute Residual  $\mathbf{r}^{(n)}$ 
    if Classical Galerkin then ▷ Solve without non-negative methodology
         $\mathbf{c}^{(n+1)} = \mathbf{c}^{(n)} - \mathbf{J} \setminus \mathbf{r}^{(n)}$ 
    else ▷ Solve with non-negative methodology
        TaoSolve() for  $\mathbf{c}^{(n+1)}$ 
    end if
    if steady-state or  $(n) ==$  total number of time steps then
        break
    else
         $n+ = 1$ 
    end if
end while

```

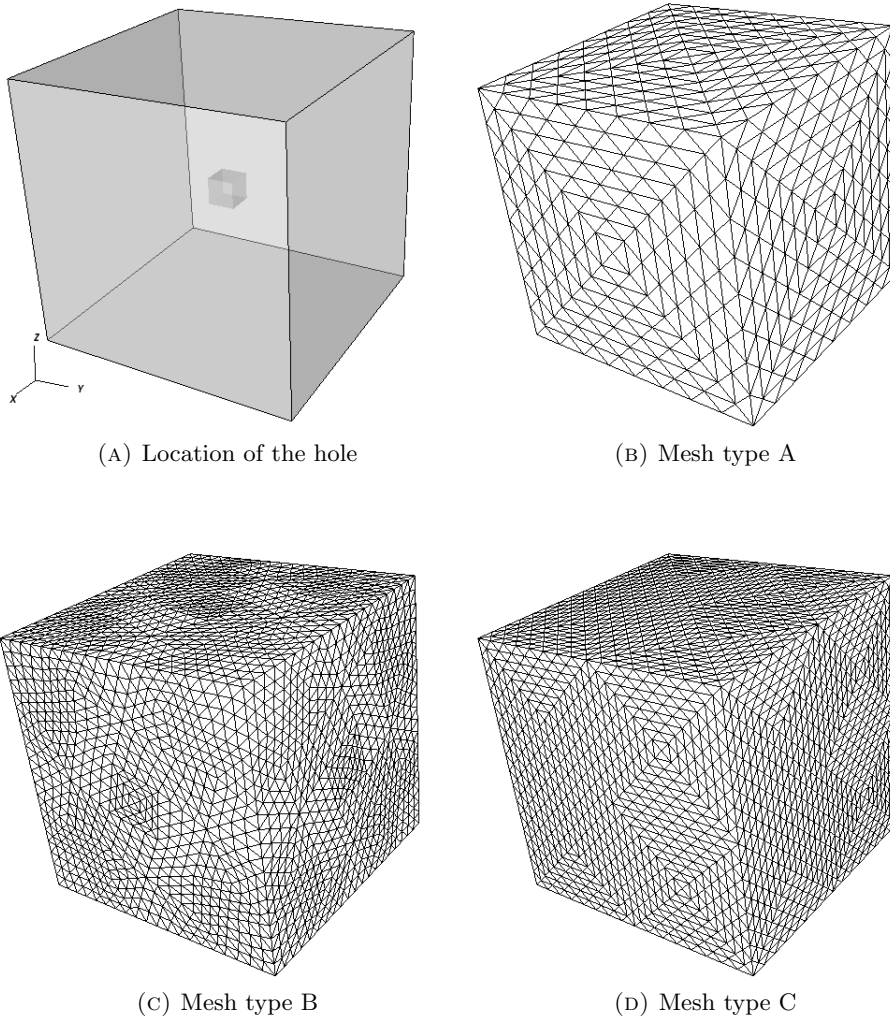


FIGURE 2. Pictorial description of the unit cube with hole problem and the associated unstructured grids.

denotes initial condition) then the residual and Jacobian can be defined as:

$$\mathbf{r}^{(n)} \equiv \mathbf{r}(\mathbf{c}^{(n)}) \quad (3.7)$$

$$\mathbf{J} \equiv \mathbf{J}(\mathbf{c}^{(0)}) \quad (3.8)$$

To enforce the non-negative methodology with the BLMVM algorithm, the following objective function b and gradient function \mathbf{g} are provided:

$$b = \frac{1}{2} \mathbf{c}^{(n+1)} \cdot \mathbf{J} \mathbf{c}^{(n+1)} + \mathbf{c}^{(n+1)} \cdot [\mathbf{r}^{(n)} - \mathbf{J} \mathbf{c}^{(n)}] \quad (3.9)$$

$$\mathbf{g} = \mathbf{J} [\mathbf{c}^{(n+1)} - \mathbf{c}^{(n)}] + \mathbf{r}^{(n)} \quad (3.10)$$

Algorithm 1 outlines the steps taken in our computational framework.

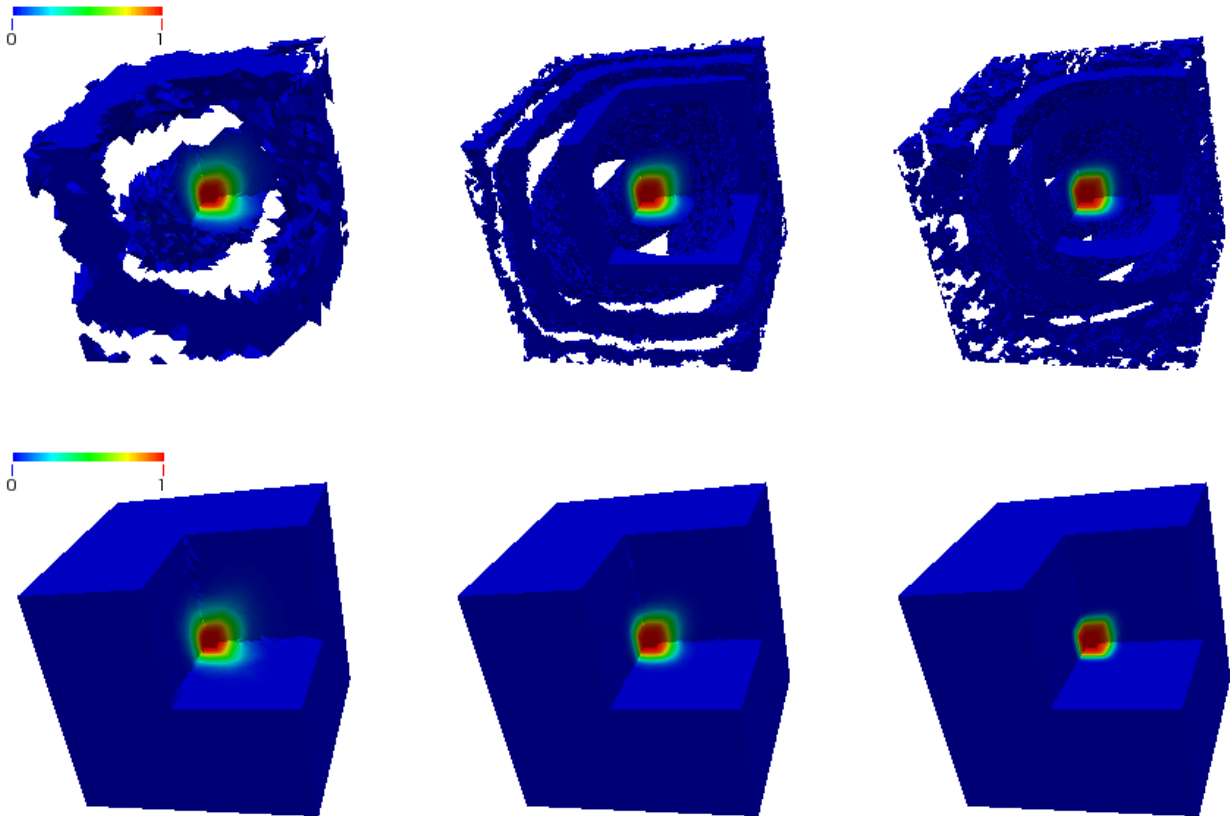


FIGURE 3. Cube with hole: numerical solution for cases A1 (left), B2 (middle), and C3 (right) using the Galerkin formulation (top row) and non-negative methodology (bottom row).

4. REPRESENTATIVE NUMERICAL RESULTS

In this section, we compare the performance of our non-negative methodology using the TAO solver to that of the Galerkin formulation using the Krylov Subspace (KSP) solver. We examine the performance using two problems:

- (i) a unit cube with a hole under steady-state, and
- (ii) a transient Chromium transport problem.

The diffusivity tensor is assumed to depend on the flow velocity through

$$\mathbf{D}(\mathbf{x}) = (\alpha_T \|\mathbf{v}\| + D_M) \mathbf{I} + (\alpha_L - \alpha_T) \frac{\mathbf{v} \otimes \mathbf{v}}{\|\mathbf{v}\|} \quad (4.1)$$

where α_L , α_T , and D_M denote the longitudinal dispersivity, transverse dispersivity and molecular diffusivity, respectively. We employ the conjugate gradient method and the Jacobi preconditioner for solving the linear system from the Galerkin formulation and employ TAO's BLMVM method for the non-negative methodology. The convergence tolerance for both solvers is set to 10^{-8} , and Δt for the transient response in the Chromium problem is set to 0.2 days. For scaling studies shown here, we used MPICH v3.1.4 for message passing on Mustang and bound all processes to cores while mapping

TABLE 2. Cube with hole: list of various mesh type and refinement level combinations used

| Case | Mesh type | Refinement level | Tetrahedrons | Vertices |
|------|-----------|------------------|--------------|-----------|
| A1 | A | 1 | 199,296 | 36,378 |
| B1 | B | 1 | 409,848 | 75,427 |
| C1 | C | 1 | 793,824 | 140,190 |
| A2 | A | 2 | 1,594,368 | 278,194 |
| B2 | B | 2 | 3,278,784 | 574,524 |
| C2 | C | 2 | 6,350,592 | 1,089,562 |
| A3 | A | 3 | 12,754,994 | 2,175,330 |
| B3 | B | 3 | 26,230,272 | 4,483,126 |
| C3 | C | 3 | 50,804,736 | 9,172,044 |

by NUMA nodes. On Wolf, we used OpenMPI v1.8.5 for message passing and bound processes to cores while mapping by sockets. ParaView [2] and VisIt [5] were used to generate all contour and mesh plots.

REMARK 1. *In this paper, we include performance metrics using the conjugate gradient solver with Jacobi preconditioner for the resulting algebraic system from the Galerkin formulation. Geometric and algebraic multigrid methods might be better for this but we are more interested in evaluating how well the TAO solver performs for the non-negative methodology.*

4.1. Anisotropic diffusion in a unit cube with a cubic hole. Let the computational domain be a unit cube with a cubic hole of size $[4/9, 5/9] \times [4/9, 5/9] \times [4/9, 5/9]$. The concentration on the outer boundary is taken to be zero and the concentration on the interior boundary is taken to be unity. The volumetric source is taken as zero (i.e., $f(\mathbf{x}) = 0$). The velocity vector field for this problem is chosen to be

$$\mathbf{v}(\mathbf{x}) = \mathbf{e}_x + \mathbf{e}_y + \mathbf{e}_z \quad (4.2)$$

The diffusion parameters are set as: $\alpha_L = 1$, $\alpha_T = 0.001$, and $D_M = 0$. The pictorial description of the computational domain and the three mesh types composed of 4-node tetrahedrons are shown in Figure 2. We consider three unstructured mesh types with three levels of element-wise mesh refinement, giving us nine total case studies of increasing problem size as shown in Table 2. Numerical results for both the Galerkin formulation and the non-negative methodology for some of the mesh cases are shown

TABLE 3. Cube with hole: minimum and maximum concentrations for each case

| Case | Min. concentration | Max. concentration | % nodes violated |
|------|--------------------|--------------------|---|
| A1 | -0.0224825 | 1.00000 | 9,518/36,378 \rightarrow 26.2% |
| B1 | -0.0139559 | 1.00000 | 32,247/43,180 \rightarrow 42.8% |
| C1 | -0.0125979 | 1.00000 | 57,272/140,190 \rightarrow 40.9% |
| A2 | -0.0311518 | 1.00103 | 82,983/278,194 \rightarrow 29.2% |
| B2 | -0.0143857 | 1.00000 | 255,640/574,524 \rightarrow 44.9% |
| C2 | -0.0119539 | 1.00972 | 453,766/1,089,562 \rightarrow 41.6% |
| A3 | -0.0258559 | 1.00646 | 643,083/2,175,330 \rightarrow 29.6% |
| B3 | -0.0115908 | 1.00192 | 2,073,934/4,483,126 \rightarrow 46.3% |
| C3 | -0.0096186 | 1.00545 | 4,932,551/9,172,044 \rightarrow 53.8% |

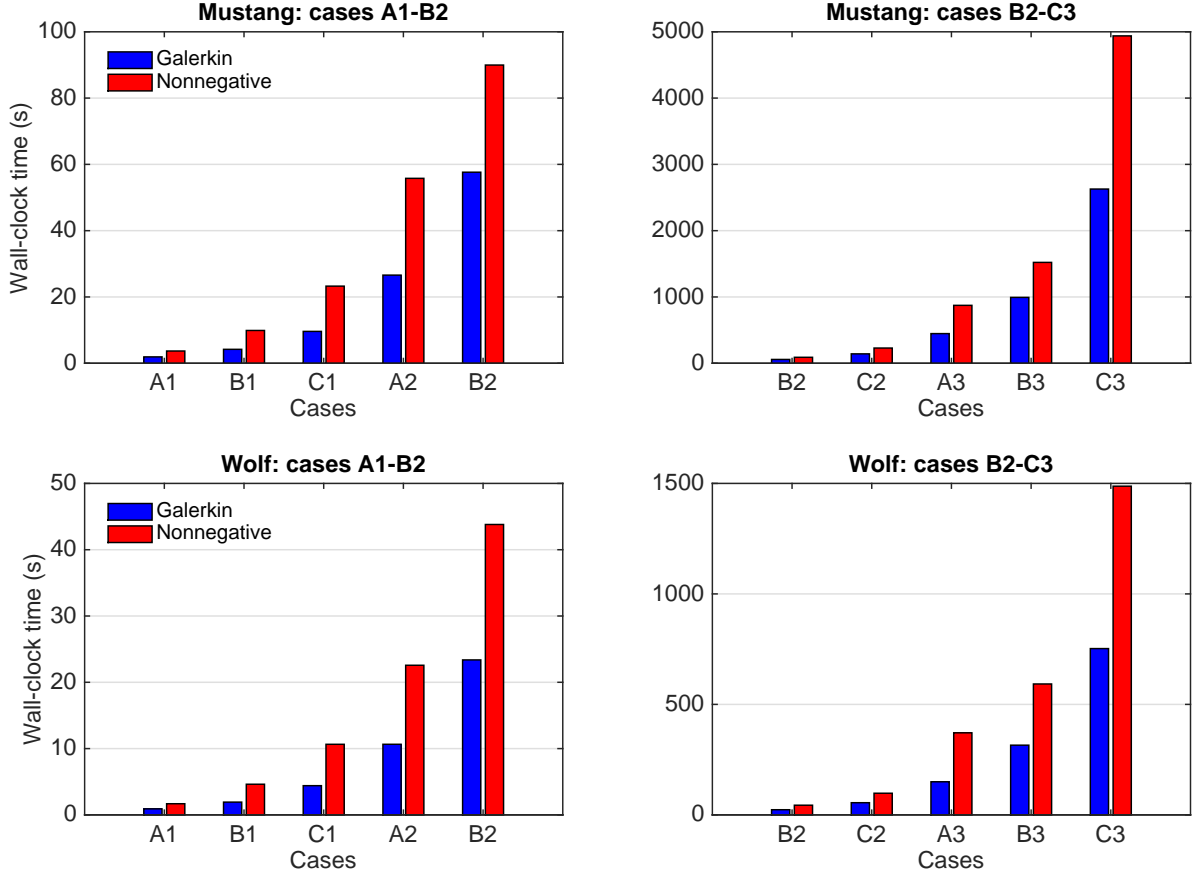


FIGURE 4. Cube with hole: wall-clock times for all solvers, problem sizes, and HPC systems on a single processor.

in Figure 3. The top set of figures are for the Galerkin formulation, where the white regions denote negative concentrations. Details concerning the violation of the DMP for each case study can be found in Table 3. Concentrations both negative and greater than one arise for all case studies. Moreover, simply refining the mesh does not resolve these issues. These numerical results indicate that our computational framework can successfully enforced the DMP for diffusion problems with highly anisotropic diffusivity.

4.1.1. *Computational Efficiency.* We now consider the wall-clock time spent in the solvers on a single processor. Figure 4 depict the solve time for each case study, and it can be seen that the Mustang system requires significantly more wall-clock time to obtain a solution than Wolf; this behavior is expected due to the difference in HPC hardware and specification listed in Table 1. It can also be seen that the non-negative methodology consumes more time and in some cases require nearly twice the amount of time of the Galerkin formulation. This begs the question: why exactly does this methodology consume more wall-clock time? Is the increase in time mostly due to additional workload associated with optimization-based technique or is the computational framework less efficient compared the one used to solve the Galerkin formulation? We begin to explore these questions by first noting the total Krylov Subspace (KSP) and TAO solve iterations needed for each method to fulfill the convergence criterion as seen in Figure 5. As with wall-clock time, the number of solver iterations generally increases with problem

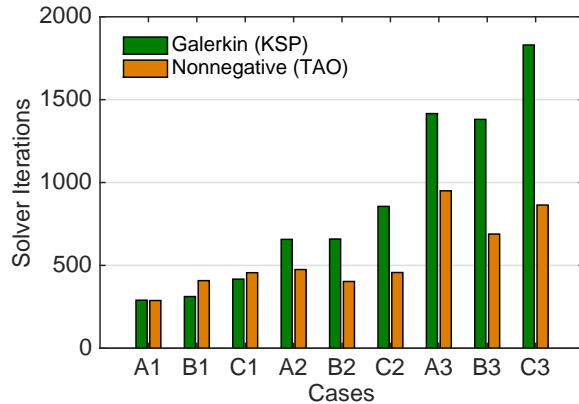


FIGURE 5. Cube with hole: solver iterations needed for convergence.

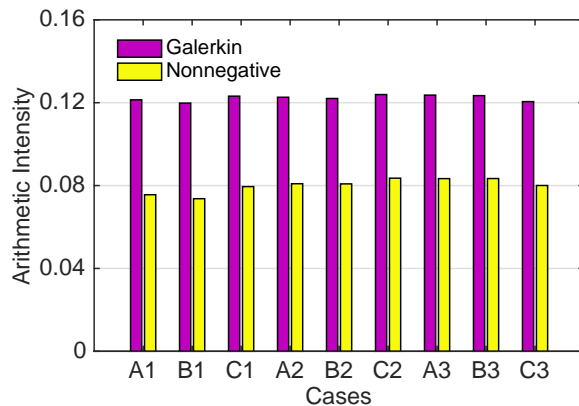
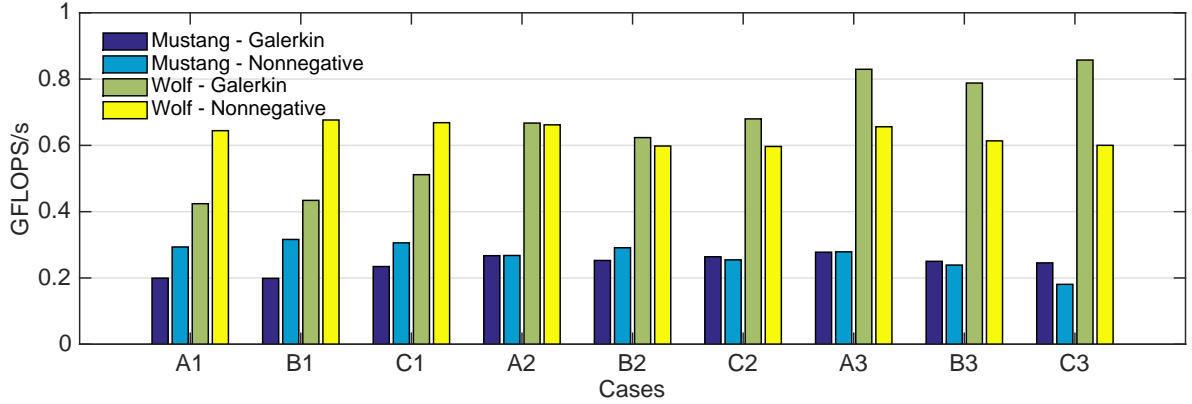


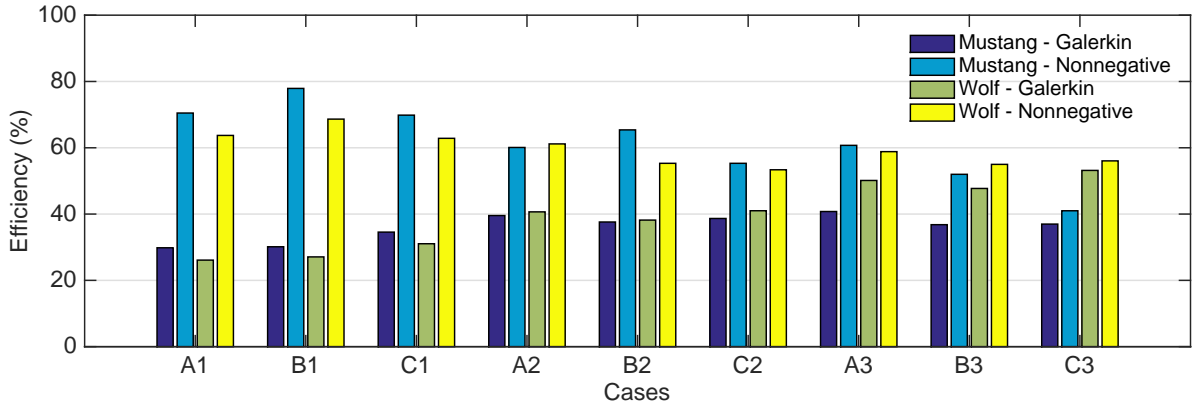
FIGURE 6. Cube with hole: arithmetic intensity for both solvers on all problem sizes on a single processor.

size, but it is not entirely uniform due to the different mesh structures and their round robin use. The increase in the number of TAO iterations is not as great as the KSP iterations, but the wall-clock timings indicate that the average time spent for each solver iteration is significantly greater in TAO.

Although both solver iterations and wall-clock time increase with problem size, the estimated AI remains largely invariant as seen in Figure 6. Optimization-based algorithms based on TAO’s BLMVM solver have more streaming operations and are less dependent on sparse matrix-vector multiplications due to the fewer amount of solve iterations. This observation is strongly correlated to why the AI is significantly higher for the KSP solver. However, this does not mean that TAO is less efficient. Figure 7 draws comparisons between the measured FLOPS/s obtained from the PETSc profiling summary output and the estimation of the ideal FLOPS/s using equation (3.1). The ideal FLOPS/s is chosen as the product of the STREAMS Triad bandwidth from Table 1 and the AI from Figure 6 because it is smaller than the TPP of the respective HPC systems. It can be seen that the floating point performance for the Galerkin formulation gradually increases with problem size while the non-negative performance remains somewhat invariant. Although the optimization-based solver has a lower AI, it has a higher



(A) Measured GFLOPS/s



(B) Relative efficiency

FIGURE 7. Cube with hole: estimations of the floating-point efficiency with respect to the measured memory bandwidth from STREAMS for all problems sizes on a single processor.

ratio of measured over ideal FLOPS/s for smaller problem sizes, hence higher efficiencies. However, as the problem size increases, the absolute difference in efficiencies reduces, indicating that the greater wall-clock times associated with the TAO solver is mostly due to additional workload.

4.1.2. *Strong-scaling.* Another metric of interest is the ability of the computational framework to efficiently scale across multiple processing cores. We conduct strong-scaling studies to measure the speedup of all nine case studies over 64 cores. Four Mustang nodes with 16 processors each and 8 Wolf nodes with 8 processors each are allocated for this study. Figure 8 depicts the speedup for all nine problem sizes on both HPC systems. The parallel efficiency (actual speedup over ideal speedup) increases with problem size and is consistent with Amdahl’s Law because the amount of work conducted locally increases hence decreasing the fraction of the computational framework that is strictly serial. An interesting observation that we note is that the TAO solver is less efficiency (in the parallel sense) than the KSP solver for small problems, but will eventually surpass KSP as the problem size grows. In fact, super-linear speedup is present in case studies B3 and C3. This change of behavior for speedup

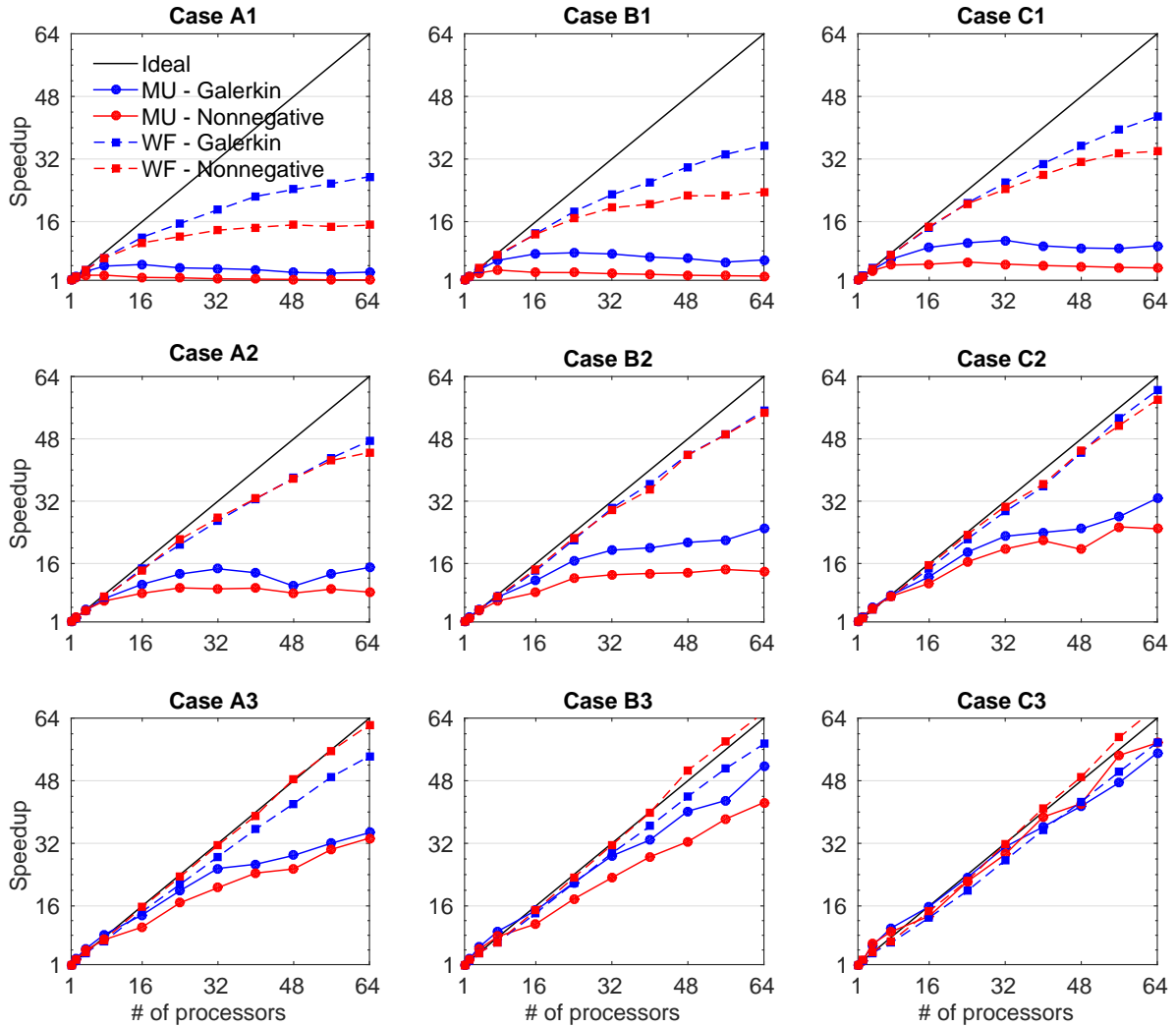


FIGURE 8. Cube with hole: speedup for up to 64 processors.

may largely be attributed to the increasing difference in solve iterations required as shown in Figure 5 (hence more communication). Our findings indicate that our non-negative framework is efficient in both the floating-point and parallel sense when working with sufficiently large problems.

4.2. Transport of chromium in subsurface. Chromium, in large amounts, can be toxic [31]. This is a primary reason why abandoned chromium sites often require environmental cleanup. Remediation studies need accurate predictions of transport of the involved chemical species, which are obtained using limited data at monitoring wells and through numerical simulations. Therefore, an accurate predictive numerical simulator that predicts the fate of a chemical species in the subsurface is of significant importance. In order to achieve this, it is important to have a transport solver that is robust and will not give unphysical solutions, and handle field-scale scenarios. The computational framework that is

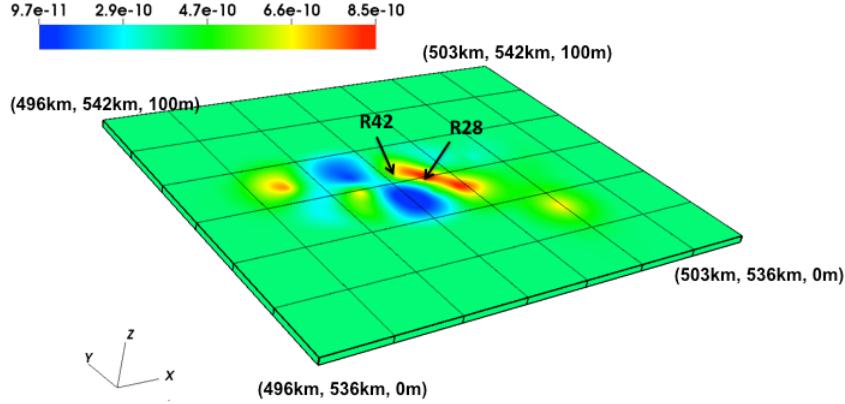


FIGURE 9. Permeability field (m^2) for the Chromium in subsurface problem and the locations of the pumping well (R28) and contaminant source (R42).

proposed in this paper is an ideal candidate for such problems. We now solve a realistic large-scale problem to predict the fate of the transport of chromium in the subsurface using the proposed computational framework.

Consider a domain of size $[496, 503]\text{km} \times [536, 542]\text{km} \times [0, 100]\text{m}$ with the permeability field (m^2) as shown in Figure 9. The parameters used for this problem are shown in Table 4, and we employ the following boundary conditions:

$$c^P(x = 496\text{km}, y, z) = c^P(x = 503\text{km}, y, z) = c^P(x, y = 536\text{km}, z) = c^P(x, y = 542\text{km}, z) = 0 \quad (4.3)$$

We first solve the elliptic Darcy equation with the pumping well (pressure source) located at R28. Cell-wise velocity is obtained from the resulting pressure field and used to calculate element-wise diffusivity. The heterogeneous diffusivity tensor propagates the dispersion of Chromium through the subsurface. We then solve the transient diffusion problem with a constant contaminant source located at R40 for 900 time levels and use up to 128 compute nodes on Wolf (2048 total processors). The concentration

TABLE 4. Chromium in subsurface: parameters

| Parameter | Value |
|--------------------------|---|
| α_L | 100 m |
| α_T | 0.1 m |
| Contaminant source (R42) | $1 \times 10^{-4} \text{ kg/m}^2\text{s}^2$ |
| Δt | 0.2 days |
| Domain size | $7000 \text{ km} \times 6000 \text{ km} \times 100 \text{ m}$ |
| D_M | $1 \times 10^{-9} \text{ m}^2/\text{s}$ |
| Permeability | Varies |
| Pumping well (R28) | $-0.01 \text{ kg/m}^2\text{s}^2$ |
| Total hexahedrons | 1,984,512 |
| Total vertices | 2,487,765 |
| \mathbf{v} | Varies |
| Viscosity | $3.95 \times 10^{-5} \text{ Pa s}$ |

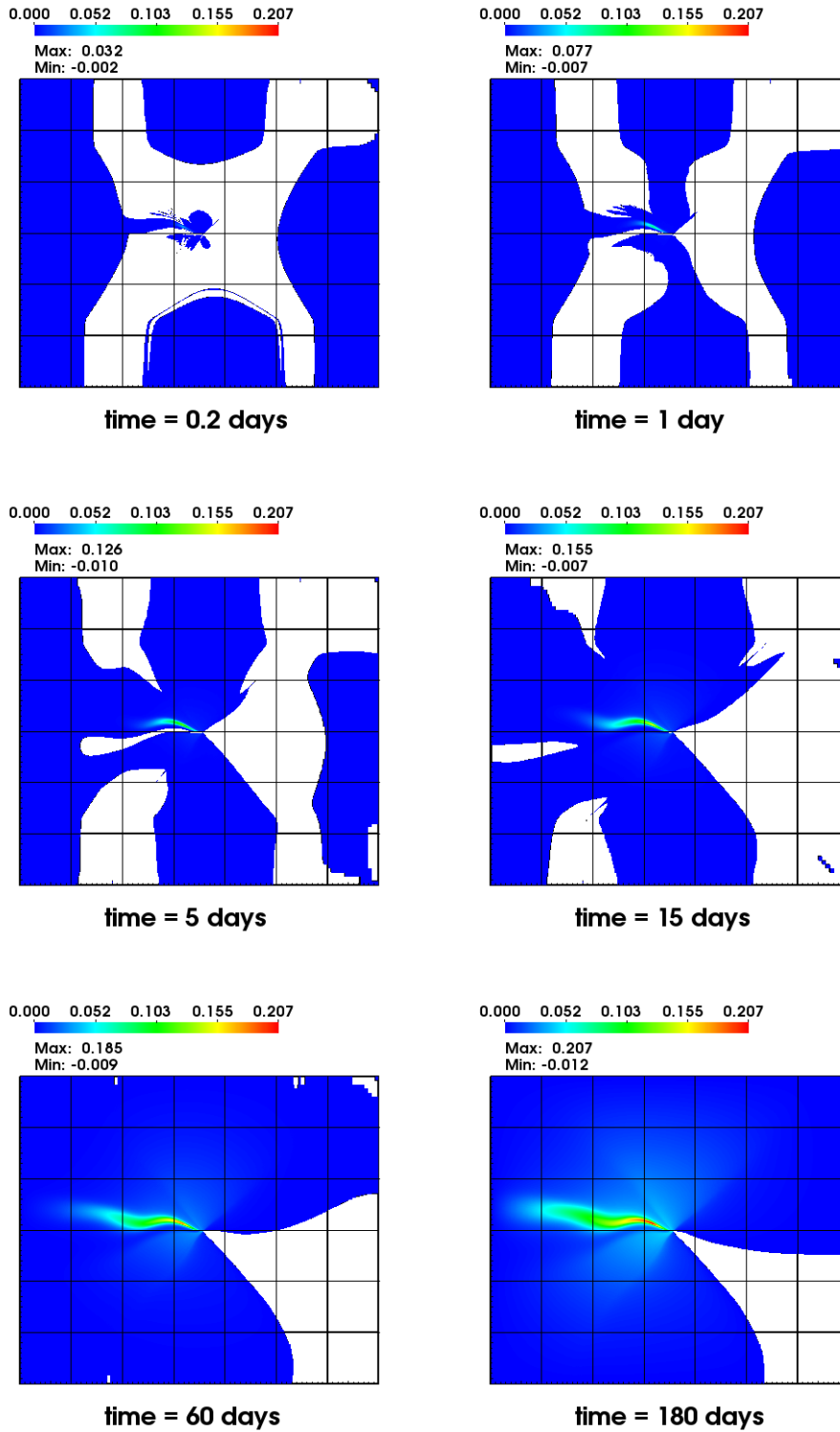


FIGURE 10. Chromium in subsurface: concentrations at select time steps using the Galerkin formulation.

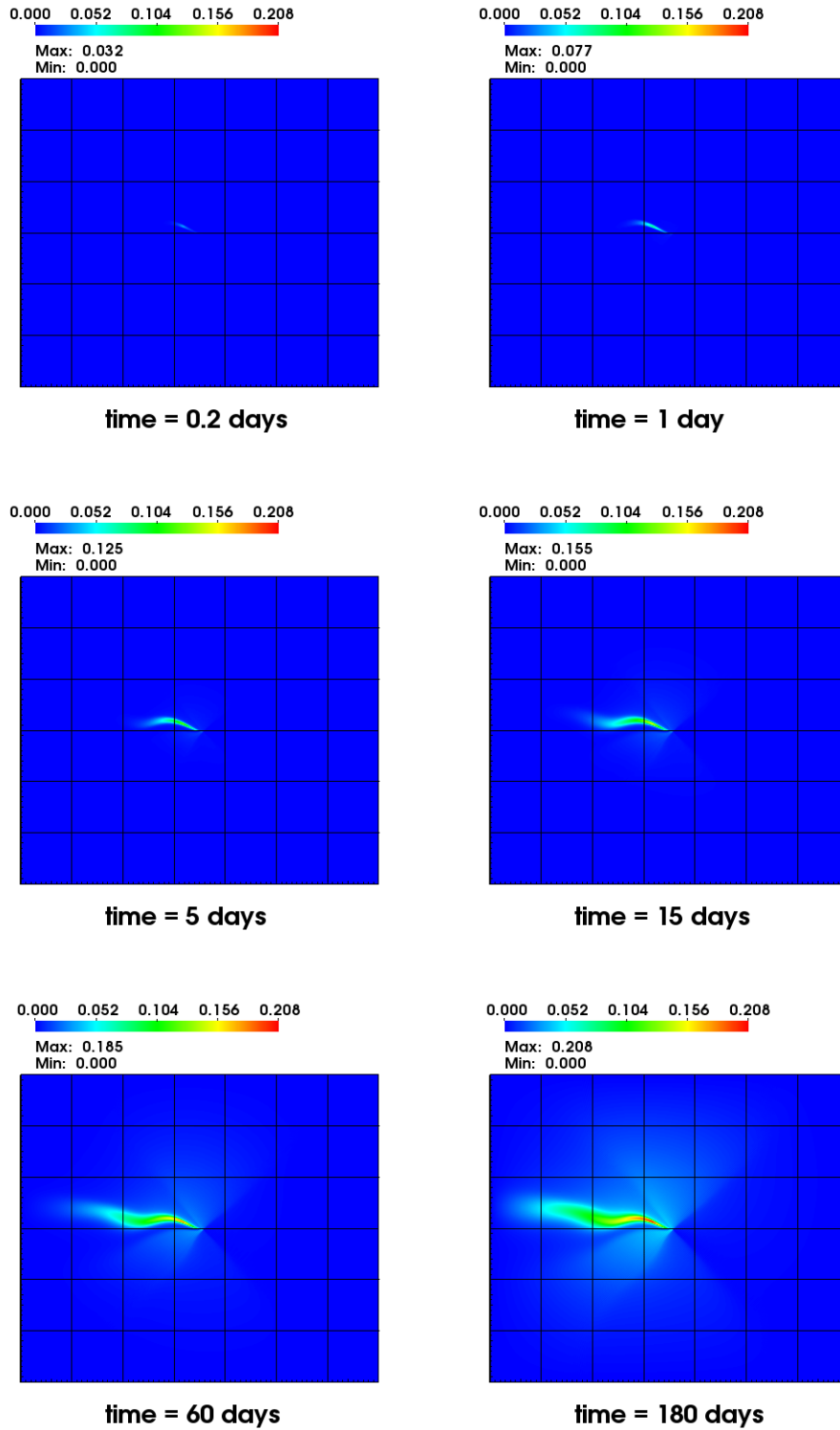


FIGURE 11. Chromium in subsurface: concentrations at select time steps using the non-negative methodology.

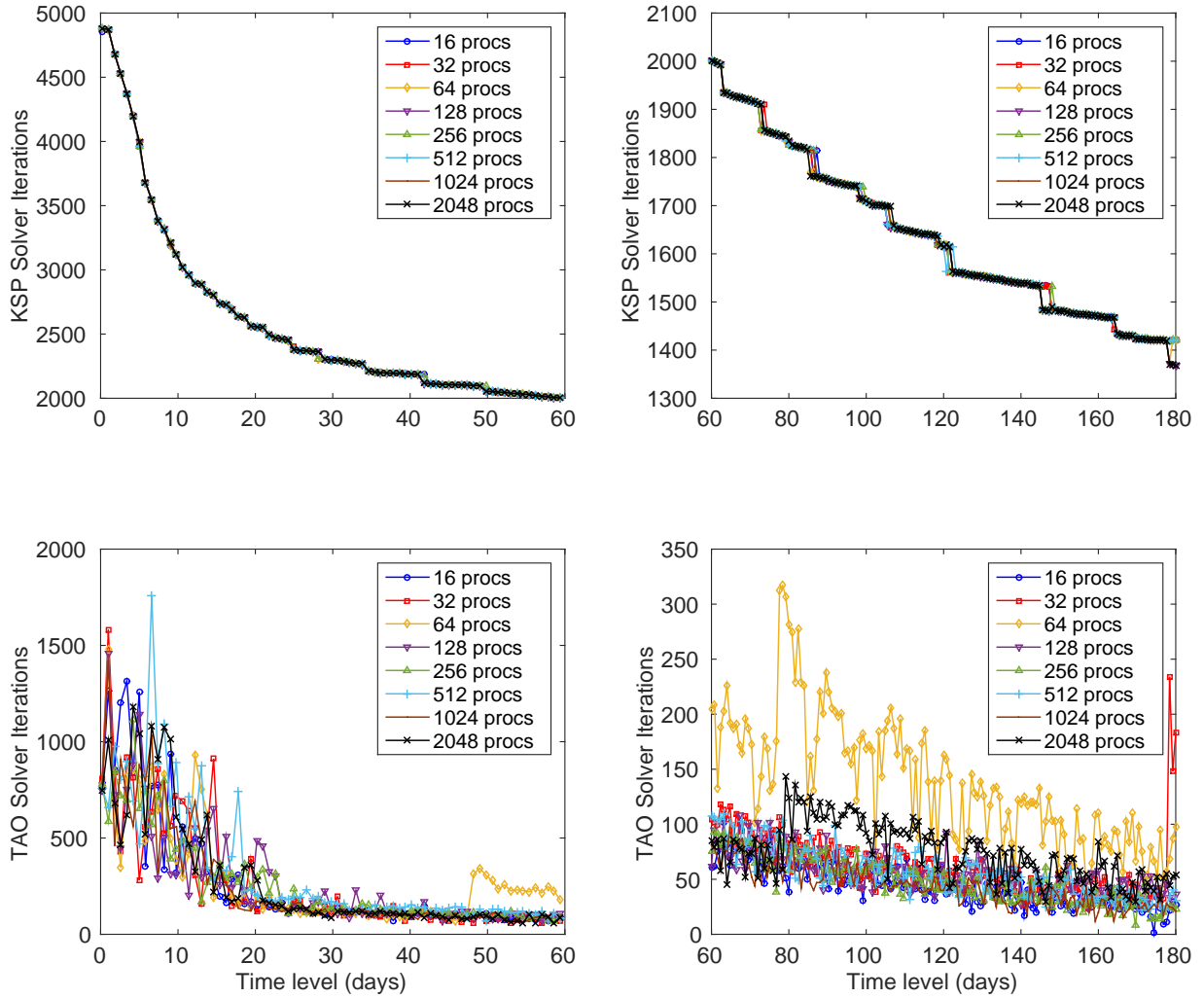


FIGURE 12. Chromium in subsurface: solver iterations required at every time level with respect to number of processors.

at select time levels is shown in Figures 10 and 11. We see that negative concentrations arise even as the solution approaches steady-state.

Figure 12 depicts the number of solver iterations at each time level with respect to the number of processors. The volumetric source is independent of time which explains why both the number of solver iterations and the magnitude of the solution update decrease as the time level increases. It is interesting to note that the number of TAO iterations fluctuates greatly at each time level when different numbers of processing cores are used; Figure 13 depicts the variational of iterations at select time levels. This behavior is largely attributed to the accumulation of numerical round-offs within the BLMVM algorithm. Although the resulting solutions are unaffected by the partition sizes, the differing number of iterations

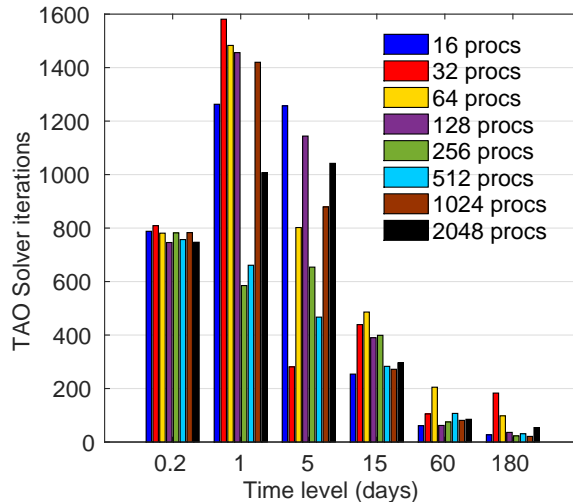


FIGURE 13. Chromium in subsurface: variation of TAO solver iterations at select time levels with respect to number of processors.

at each time level greatly affects the trend of the wall-clock times in Figure 14. It is difficult to draw any conclusions about strong-scaling from these figures alone so we measure the total wall-clock time across all 900 time levels in Figure 15. This figure indicates that we have achieved excellent strong-scaling across 512 processors despite the seemingly erratic behavior of the solver iterations at every time level. Moreover, the TAO solver outperforms the CG/Jacobi combination in terms of wall-clock time. This difference in wall-clock time is completely different from what we have observed for the steady-state cube problem. We see from Figure 16 that the measured floating-point performance of the TAO solver is smaller, suggesting that the reason for greater wall-clock times observed with the Galerkin formulation has less to do with computational inefficiency. Nonetheless, this study suggests that the non-negative methodology built upon the PETSc and TAO libraries is particularly suited for parabolic-like equations and is a viable option to ensure the DMP for large-scale and transient diffusion problems.

5. CONCLUDING REMARKS

We presented a parallel non-negative computational framework suitable for solving large-scale steady-state and transient anisotropic diffusion equations. The main contribution is that the proposed parallel computational framework satisfies the non-negative constraint and maximum principles for large-scale diffusion-type equations even on general computational grids. The parallel framework is built upon PETSc’s DMplex data structure, which can handle unstructured meshes, and TAO for solving the resulting optimization problems. We have performed a systematic strong scaling and efficiency studies, and the proposed parallel computational framework has shown strong excellent performance. The robustness of the proposed framework has been illustrated by solving a large-scale realistic problem involving the transport of chromium in subsurface. A logical next step of this research work is to extend the proposed parallel framework to advective-diffusive and advective-diffusive-reactive systems.

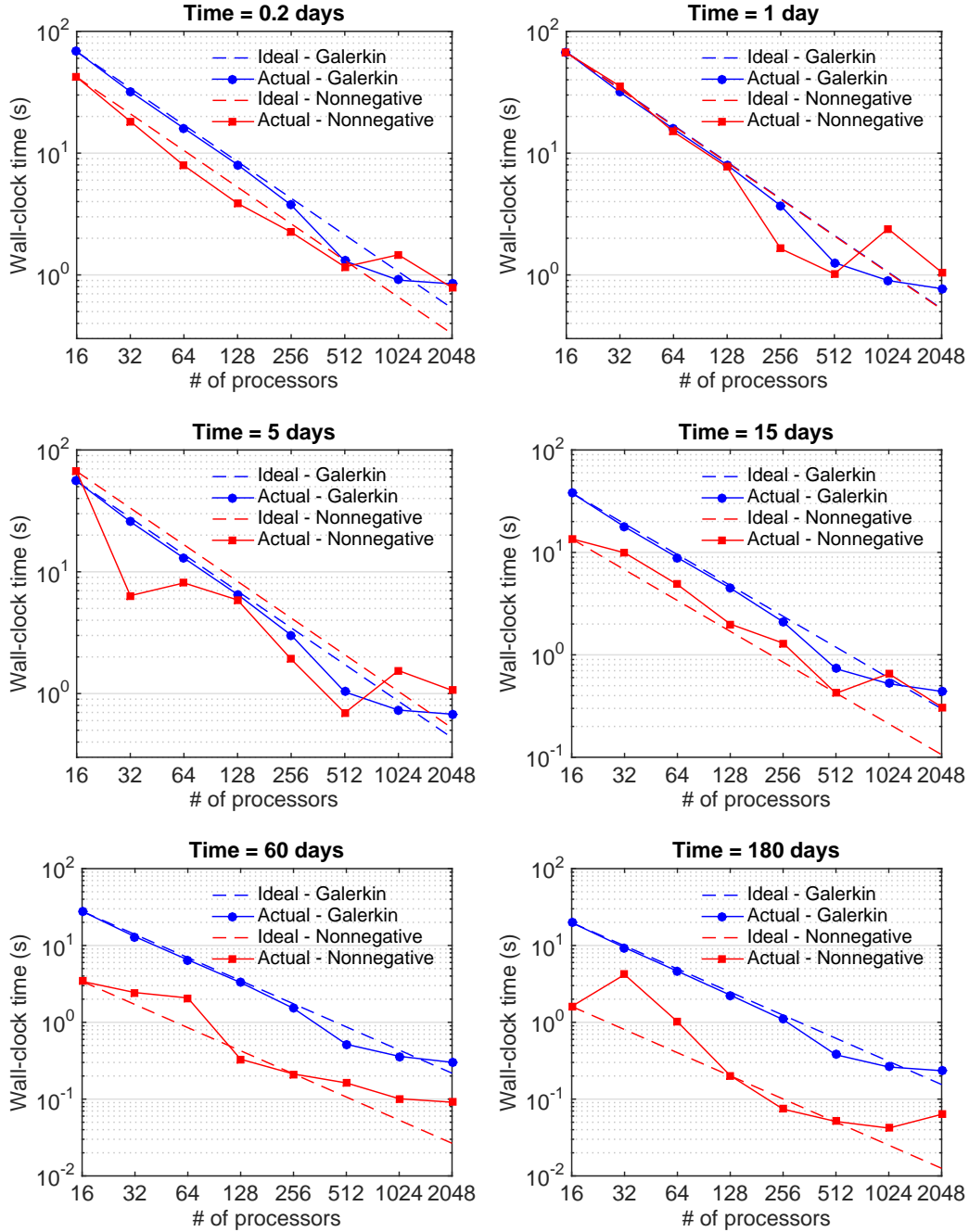


FIGURE 14. Chromium in subsurface: wall-clock time at select time steps versus number of processors on the Wolf system.

ACKNOWLEDGMENTS

The authors thank Matthew G. Knepley (Rice University) for his invaluable advise. JC and KBN acknowledge the financial support from the Department of Energy through Subsurface Biogeochemical Research Program, and the Houston Endowment. SK thanks the Los Alamos National Laboratory

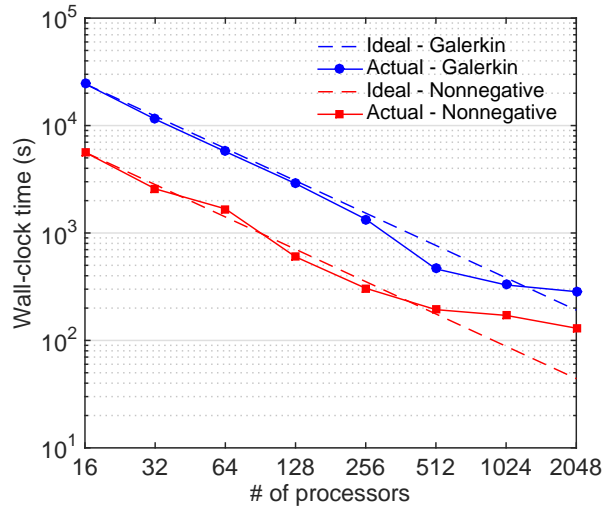


FIGURE 15. Chromium in subsurface: total wall-clock time versus number of processors on the Wolf system.

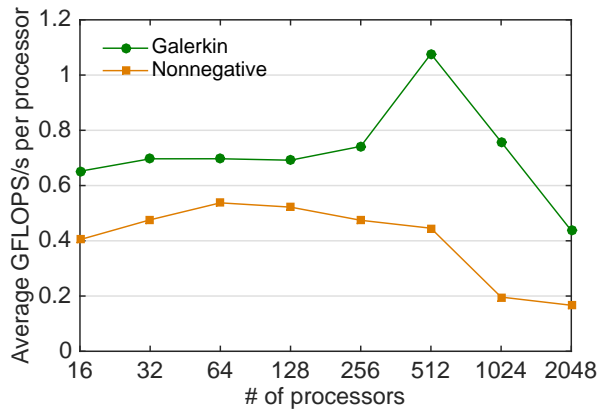


FIGURE 16. Chromium in subsurface: average floating point performance per processor on the Wolf system.

(LANL) LDRD program and the DOE FE program for their support. The opinions expressed in this paper are those of the authors and do not necessarily reflect that of the sponsors.

References

- [1] Robert A Adams and John JF Fournier. *Sobolev spaces*, volume 140. Academic press, 2003.
- [2] U. Ayachit. *The ParaView Guide: A Parallel Visualization Application*. Kitware, 2015.
- [3] S. Balay, S. Abhyankar, M. F. Adams, J. Brown, P. Brune, K. Buschelman, V. Eijkhout, W. D. Gropp, D. Kaushik, M. G. Knepley, L. C. McInnes, K. Rupp, B. F. Smith, S. Zampini, and H. Zhang. PETSc users manual. Technical Report ANL-95/11 - Revision 3.6, Argonne National Laboratory, 2015.
- [4] S. Boyd and L. Vandenberghe. *Convex Optimization*. Cambridge University Press, Cambridge, UK, 2004.

- [5] H. Childs, E. Brugger, B. Whitlock, J. Meredith, S. Ahern, D. Pugmire, K. Biagas, M. Miller, C. Harrison, G. H. Weber, H. Krishnan, T. Fogal, A. Sanderson, C. Garth, E. W. Bethel, D. Camp, O. Rübel, M. Durant, J. M. Favre, and P. Navrátil. VisIt: An End-User Tool For Visualizing and Analyzing Very Large Data. In *High Performance Visualization—Enabling Extreme-Scale Scientific Insight*, pages 357–372. 2012.
- [6] P. G. Ciarlet and P-A. Raviart. Maximum principle and uniform convergence for the finite element method. *Computer Methods in Applied Methods and Engineering*, 2:17–31, 1973.
- [7] L. C. Evans. *Partial Differential Equations*. American Mathematical Society, Providence, Rhode Island, USA, 1998.
- [8] W. D. Gropp, D. K. Kaushik, D. E. Keyes, and B. F. Smith. Toward realistic performance bounds for implicit cfd codes. In *Proceedings of Parallel CFD’99*, pages 233–240. Elsevier, 1999.
- [9] G. E. Hammond and P. C. Lichtner. Field-scale model for the natural attenuation of uranium at the hanford 300 area using high-performance computing. *Water Resources Research*, 46(9), 2010.
- [10] K. D. Hjelmstad. *Fundamentals of Structural Mechanics*. Springer Science+Business Media, Inc., New York, USA, second edition, 2005.
- [11] J. McCalpin. STREAM: Sustainable memory Bandwidth in High Performance Computers, 1995. <https://www.cs.virginia.edu/stream/>.
- [12] S. Karra, S. L. Painter, and P. C. Lichtner. Three-phase numerical model for subsurface hydrology in permafrost-affected regions (PFLOTRAN-ICE v1. 0). *The Cryosphere*, 8(5):1935–1950, 2014.
- [13] G. Karypis and V. Kumar. A Fast and Highly Quality Multilevel Scheme for Partitioning Irregular Graphs. *SIAM Journal on Scientific Computing*, 20:359–392, 1999.
- [14] S. Kelkar, K. Lewis, S. Karra, G. Zvoloski, S. Rapaka, H. Viswanathan, P. K. Mishra, S. Chu, D. Coblenz, and R. Pawar. A simulator for modeling coupled thermo-hydro-mechanical processes in subsurface geological media. *International Journal of Rock Mechanics and Mining Sciences*, 70:569–580, 2014.
- [15] R. C. Kirby. *FIAT: Numerical Construction of Finite Element Basis Functions*, chapter 13. Springer, 2012.
- [16] M. G. Knepley, J. Brown, K. Rupp, and B. F. Smith. Achieving High Performance with Unified Residual Evaluation. *arXiv:1309.1204*, September 2013.
- [17] M. G. Knepley and D. A. Karpeev. Mesh algorithms for PDE with vieve I: Mesh distribution. *Scientific Programming*, 17:215–230, 2009.
- [18] P. C. Lichtner, G. E. Hammond, C. Lu, S. Karra, G. Bisht, B. Andre, R. T. Mills, and J. Kumar. PFLOTRAN user manual. Technical report, http://www.pflotran.org/docs/user_manual.pdf (last access: January 2015), 2013.
- [19] P. C. Lichtner and S. Karra. Modeling multiscale-multiphase-multicomponent reactive flows in porous media: Application to CO₂ sequestration and enhanced geothermal energy using pflotran. In R. Al-Khoury and J. Bundschuh, editors, *Computational Models for CO₂ Geo-sequestration & Compressed Air Energy Storage*, pages 81–136. CRC Press, <http://www.crcnetbase.com/doi/pdfplus/10.1201/b16790-6>, 2014.
- [20] R. Liska and M. Shashkov. Enforcing the discrete maximum principle for linear finite element solutions of second-order elliptic problems. *Communications in Computational Physics*, 3(4):852–877, 2008.
- [21] Y. J. Lo, S. Williams, B. V. Straalen, T. J. Ligocki., M. J. Cordery, N. J. Wright, M. W. Hall, and L. Oliker. Roofline: an insightful visual performance model for multicore architectures. *High Performance Computing Systems. Performance Modeling, Benchmarking, and Simulation*, 8966:129–148, 2015.
- [22] A. Logg. Efficient Representation of Computational Meshes. *International Journal of Computational Science and Engineering*, 4:283–295, 2009.
- [23] A. Logg, K. A. Mardal, G. N. Wells, et al. *Automated Solution of Differential Equations by the Finite Element Method*. Springer, 2012.
- [24] M. K. Mudunuru and K. B. Nakshatrala. On enforcing maximum principles and achieving element-wise species balance for advection-diffusion-reaction equations under the finite element method. *Available on arXiv: 1506.06099*, 2015.
- [25] M. K. Mudunuru and K. B. Nakshatrala. On mesh restrictions to satisfy comparison principles, maximum principles, and the non-negative constraint: Recent developments and new results. *Available on arXiv: 1502.06164*, 2015.
- [26] T. Munson, J. Sarich, S. Wild, S. Benson, and L. C. McInnes. TAO 2.0 users manual. Technical Report ANL/MCS-TM-322, Mathematics and Computer Science Division, Argonne National Laboratory, 2012. <http://www.mcs.anl.gov/tao>.
- [27] H. Nagarajan and K. B. Nakshatrala. Enforcing the non-negativity constraint and maximum principles for diffusion with decay on general computational grids. *International Journal for Numerical Methods in Fluids*, 67:820–847, 2011.

- [28] K. B. Nakshatrala, M. K. Mudunuru, and A. J. Valocchi. A numerical framework for diffusion-controlled bimolecular-reactive systems to enforce maximum principles and the non-negative constraint. *Journal of Computational Physics*, 253:278–307, 2013.
- [29] K. B. Nakshatrala, H. Nagarajan, and M. Shabouei. A numerical methodology for enforcing maximum principles and the non-negative constraint for transient diffusion equations. *arXiv:1206.0701*, 2013.
- [30] K. B. Nakshatrala and A. J. Valocchi. Non-negative mixed finite element formulations for a tensorial diffusion equation. *Journal of Computational Physics*, 228:6726–6752, 2009.
- [31] Jerome O Nriagu and Evert Nieboer, editors. *Chromium in the Natural & Human Environments*, volume 20. John Wiley & Sons, 1988.
- [32] G. S. Payette, K. B. Nakshatrala, and J. N. Reddy. On the performance of high-order finite elements with respect to maximum principles and the nonnegative constraint for diffusion-type equations. *International Journal for Numerical Methods in Engineering*, 91:742–771, 2012.
- [33] K. Pruess. The TOUGH codes—a family of simulation tools for multiphase flow and transport processes in permeable media. *Vadose Zone Journal*, 3(3):738–746, 2004.
- [34] The HDF Group. Hierarchical Data Format, version 5, 1997-2015. <http://www.hdfgroup.org/HDF5/>.
- [35] S. Williams, A. Waterman, and D. Patterson. Roofline: an insightful visual performance model for multicore architectures. *Communications of the ACM*, 52:65–76, 2009.
- [36] G. Zyvoloski. FEHM: A control volume finite element code for simulating subsurface multi-phase multi-fluid heat and mass transfer. *Los Alamos Unclassified Report LA-UR-07-3359*, 2007.